# Spin-dependent Dirac electrons and valley polarization in the ferromagnetic stanene/CrI₃ van der Waals heterostructure

Baoxing Zhai [ORCID],[1] Juan Du,[2] Chenhai Shen,[1] Tianxing Wang,[1] Yuting Peng,[3] Qiming Zhang [ORCID],[3] and Congxin Xia [ORCID][1,*]

[1]*School of Physics, Henan Normal University, Xinxiang 453007, China*
[2]*State Key Laboratory for Artificial Microstructures and Mesoscopic Physics, School of Physics,*
*Peking University, Beijing 100871, China*
[3]*Department of Physics, University of Texas at Arlington, Texas 76019, USA*

Realization and regulation of valley polarization is a core issue in the valleytronics fields. Here, through first-principles calculations, we find that the valley polarization (up to 39.6 meV) can be realized in stanene, by stacking it on a monolayer ferromagnetic insulator CrI₃, forming the ferromagnetic stanene/CrI₃ van der Waals heterostructure. The heterostructure possesses a magneto band-structure effect, whereby the spin orientation of Cr atoms can significantly influence valley polarization. When the spin orientation of Cr atoms is parallel (perpendicular) to the $c$ axis, the largest (smallest) valley polarization is achieved with the value of 71.7 meV (1.7 meV). Additionally, the spin-polarized Dirac electrons and hole doping are induced in stanene due to the magnetic proximity effect, and the Dirac cone of stanene is opened with the value of 187.6 meV. These results indicate that the stanene/CrI₃ heterostructure is very promising to be applied in future spintronics and valleytronics.

## I. INTRODUCTION

Recently, two-dimensional (2D) valleytronic materials are becoming an exciting research topic in condensed matter physics and materials fields, as they provide a good platform to explore valley physics and utilize the valley index for device applications [1–11]. Therefore, the valley-physics properties of graphene and monolayer transition metal dichalcogenides (TMDC) $MX_2$ ($M$ = Mo, W; $X$ = S, Se, Te) have been extensively studied [1,2]. Compared with graphene, monolayer $MX_2$ has stronger spin orbit coupling (SOC) effects, which lead to obvious energy level splitting at $K$ and $K'$ valleys, and the two valleys are energetically degenerate in intrinsic monolayer $MX_2$ because of the time-reversal symmetry. Also, the broken inversion symmetry of monolayer $MX_2$ can implement the valley Hall effect, where carriers in different valleys flow to opposite transverse edges when applying an in-plane electric field [5,6].

Moreover, when we introduce a nonzero net magnetic moment in this material, the valley degeneracy can be removed, and we call it the valley polarization. At present, several methods are often used to realize valley polarization, such as optical pumping [12,13], external magnetic field [14–16], doping magnetic atoms [17], constructing ferromagnetic (FM) heterostructures [18–23]. Among them, constructing FM heterostructures is a very promising method because it is more stable and easier to regulate.

For heterostructure engineering, previous research mainly focus on the mixed dimensional (2D/3D) heterostructures formed by stacking monolayer TMDC or graphene on FM or antiferromagnetic (AFM) bulk materials, such as MoTe₂/EuO

[18], MoS₂/EuS [19] and WS₂/MnO [20]. In recent years, with the emergence of 2D FM materials [24–26], people have begun to study valley polarization in 2D/2D systems [27–33]. For example, Liu *et al.* have studied the effect of the stacking mode on valley polarization in WSe₂/CrI₃ heterostructure [27]. Farooq *et al.* found that the valley polarization exists in graphene/CrI₃ and bilayer graphene/CrI₃ heterostructures, and the valley-polarization characteristics can be regulated by electric field [31]. However, it should be pointed out that although valley polarization has been found in these systems, the degree of polarization is very small, which is not conducive to practical application. Thus, we need to continue searching materials that can generate larger valley polarization.

We notice that stanene is a layered material similar to graphene, where the stannum atom has the same valence electron number as carbon atom. Thus, as expected, stanene possesses similar properties as graphene, such as Dirac cones and high carrier mobility [34,35]. Compared with graphene, stanene owns a buckling crystal structure, which reduces its symmetry. Moreover, its larger atomic number indicates a stronger SOC effect. However, up to now, research about the valley-physics properties of stanene are still very rare [36].

In this work, by stacking stanene on a FM monolayer insulator CrI₃, we find that the valley polarization was realized in stanene/CrI₃ with the value of valley polarization reaching 39.6 meV. Moreover, the spin orientation of Cr atoms can significantly regulate the degree of valley polarization. Due to the magnetic proximity effect, the spin-polarized Dirac electrons and hole doping are induced in stanene with a band gap of 187.6 meV opened in the Dirac cone. By calculating the binding energy and total energy of the FM and AFM states, we confirm that the stanene/CrI₃ heterostructure is stable and possesses the FM ground state. These results indicate that the

*Corresponding author: xiacongxin@htu.edu.cn

stanene/CrI$_3$ heterostructure is very promising to be applied in future 2D high-performance spintronic and valleytronic devices.

## II. METHODS

For the studies of total energy and electronic structures, we perform the density functional theory (DFT) calculations implemented in the Vienna *ab initio* simulation package [37]. The exchange correlation potential is described with the Perdew-Burke-Ernzerhof of the generalized gradient approximation (GGA) [38]. To take into account of the correlation effects of Cr 3$d$ electrons, the GGA+$U$ method is adopted [39], and the value of the on-site Coulomb interaction $U$ and exchange interaction $J$ are set to be 3.0 and 0.9 eV, respectively [40]. The electron-ion potential is described by the projected augmented wave [41]. The kinetic energy cutoff of the plane wave is set to be 400 eV for the plane wave expansion. The Brillouin zone integration is carried out using $13 \times 13 \times 1$ and $7 \times 7 \times 1$ Monkhorst-Pack $k$-point meshes for geometry optimization of stanene (CrI$_3$) monolayer and stanene/CrI$_3$ heterostructure, respectively [42]. All geometric structures are fully relaxed until energy and forces are converged to $10^{-5}$ eV and 0.01 eV/Å, respectively. The SOC effect [43] is included in the calculations. Meanwhile, the van der Waals interaction in the stanene/CrI$_3$ heterostructure system are corrected by using the semiempirical DFT-D3 method, which gives a good description of long-range vdW interactions [44,45]. Moreover, the thickness of vacuum region is set to larger than 15 Å to avoid spurious interaction between the periodically repeated systems.

## III. RESULTS AND DISCUSSIONS

For the isolated stanene and monolayer CrI$_3$, the geometric and electronic structures are studied, as shown in Fig. S1 of the Supplemental Material [46]. The results show that both stanene and monolayer CrI$_3$ share the similar hexagonal structure, and the lattice constants are 4.673 and 7.060 Å for stanene and CrI$_3$, respectively. Monolayer CrI$_3$ is calculated to be a ferromagnetic insulator with a magnetic moment of 6 $\mu_B$/per unit cell. Moreover, when considering the SOC effect, we find that the valence band of CrI$_3$ has a distinct band splitting at the $\Gamma$ point, which reduces the band gap of monolayer CrI$_3$ obviously (see Fig. S1(c) in the Supplemental Material [46]). In addition, stanene has a Dirac cone similar to graphene at $K$ and $K'$ high symmetry points, while its Dirac cone can be opened with a bandgap of 73.8 meV near the Fermi level when considering the SOC effect (see Fig. S1(d) in the Supplemental Material [46]). These results agree well with previous researches [34,40,47].

### A. Structure model and stability of stanene/CrI$_3$ heterostructure

Here, the perpendicular stanene/CrI$_3$ bilayer heterostructure is built by stacking the stanene onto the CrI$_3$ monolayer. To reduce the lattice mismatch between the stanene and CrI$_3$ layers, we adopt the $\sqrt{3} \times \sqrt{3}$ CrI$_3$ and $\sqrt{7} \times \sqrt{7}$ stanene supercells to build the heterostructure. The calculated lattice mismatch is only 0.55% using the formula $\eta = \frac{|a_1 - a_2|}{a_1 + a_2}$, where $a_1$ and $a_2$ are the lattice constants of the corresponding
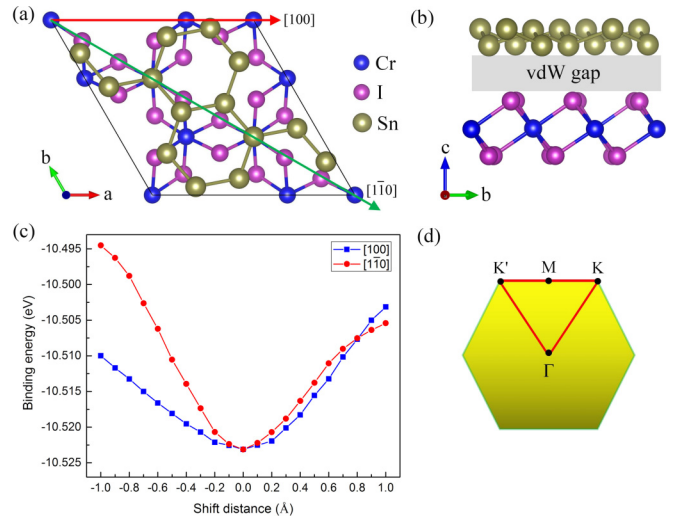


FIG. 1. The (a) top and (b) side views of stanene/CrI$_3$ heterostructure. The green and red arrows in (a) represent the shift directions, and the gray area in (b) represents equilibrium interlayer distance. (c) The binding energy as a function of the shift distance along the [100] and [1$\bar{1}$0] directions in stanene/CrI$_3$ heterostructure. (d) The first Brillouin zone and high symmetry points of the system.

stanene and CrI$_3$ supercells, respectively. The whole system consists of 38 atoms with 14 stannum atoms, six chromium atoms and 18 iodine atoms. To explore the lattice mismatch-induced strain effects on the electronic structures of each component, we examine the band structures of stanene and CrI$_3$ monolayer under the 0.55% strain (see Fig. S2 in the Supplemental Material [46]). The results show that lattice mismatch has little effects on the band structures of two isolated materials.

Considering the importance of structural symmetry for heterostructure, different stacking orders are simulated by shifting stanene layer relative to CrI$_3$ layer along [100] and [1$\bar{1}$0] directions, respectively, as shown in Fig. 1(a). The stability can be estimated by the binding energy, using the equation $E_b = E_{\text{Total}} - E_{\text{stanene}} - E_{CrI_3}$, where $E_{\text{Total}}$, $E_{\text{stanene}}$ and $E_{CrI_3}$ are the total energy of stanene/CrI$_3$ heterostructure, stanene and CrI$_3$ monolayer, respectively. Here, we systematically study the binding energy, magnetic moment, magnetism of ground state, and band structures of stanene/CrI$_3$ heterostructure under different stacking orders. The calculated results indicate that the binding energy of heterostructure is robust to the stacking orders with the value of its variation in the magnitude of meV, see Fig. 1(c). The calculated equilibrium interlayer distances under different stacking orders are about 3.2 Å, which is larger than the sum of the covalent radii of Sn atom (1.41 Å) and I atom (1.33 Å), indicating there is no chemical bonds between $MX_2$ and CrI$_3$ layers, and a typical van der Waals interaction in stanene/CrI$_3$ heterostructure [48]. Moreover, we also find that different stacking orders have little effects on the electronic structures, total magnetic moment, and the energy difference between FM and AFM states of stanene/CrI$_3$ heterostructure (see the Supplemental Material [46] for details). The stanene/CrI$_3$ van der Waals heterostructure (vdWH) always keeps the FM ground state under different stacking orders, and the stacking mode has
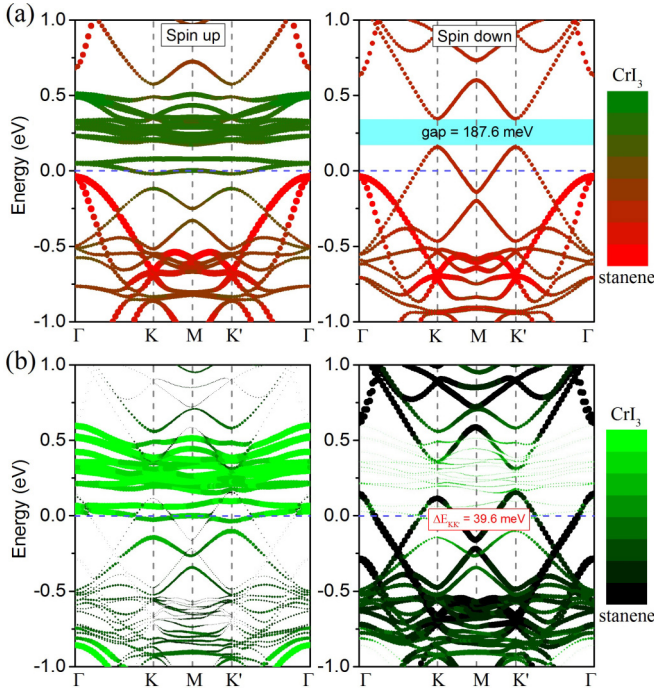
FIG. 2. (a) The spin-dependent PBS of stanene/CrI$_3$ FM vdWH without SOC effect in (left) spin-up and (right) spin-down channels. The sizes of the red and green colors represent the projected weight of stanene and CrI$_3$ components, respectively. (b) The PBS of stanene/CrI$_3$ FM vdWH with SOC effect. The sizes of the black and green colors represent the projected weight of stanene and CrI$_3$ components, respectively. The left is the PBS of CrI$_3$ and the right is the PBS of stanene. The red value insert in the right band is the value of valley polarization ($\Delta E_{KK'}$). The Fermi level is set as zero.

little effect on its band structures. Therefore, in the following calculations, we will take the most stable structure of the heterostructure [see Fig. 1(a)] as an example to further explore the physical properties of stanene/CrI$_3$ FM vdWH.

## B. Spin polarized Dirac electrons and valley polarization in stanene/CrI$_3$ FM vdWH

Now let us investigate the band structure of stanene/CrI$_3$ FM vdWH, which is very important to understand the physical properties of materials. As shown in Fig. 1(d), the band structure is calculated along the $\Gamma$-$K - M - K'$-$\Gamma$ path in the first Brillouin Zone. We first provide the band structure of stanene/CrI$_3$ FM vdWH with different stacking orders in Fig. S4 of the Supplemental Material [46]. Therefore, the red and blue lines represent the spin-up and spin-down band structures, respectively, which shows that the heterostructure possesses spin-polarized electronic structures, agreeing well with the above calculation of FM ground state.

Furthermore, in Fig. 2(a), we present the spin-dependent projected band structures (PBS) of stanene/CrI$_3$ FM vdWH for different spin channels without SOC effect. Interestingly, we find that the Dirac cone of stanene only appears in the spin-down band channel, which implies that the Dirac electrons of stanene contribute mainly from spin-down state. Similarly, very recently, Dedkov reported that the spin-polarized Dirac electron behavior exist in grapheme-Mn$_5$Ge$_3$ interface [49].

Moreover, we also find that the Dirac cone is opened with an obvious gap of 187.6 meV and it shifts upward by 157.4 meV respect to the Fermi level in spin-down channel. Meanwhile, the band of CrI$_3$ shifts downward by 21.2 meV with respect to the Fermi level in the spin-up channel. These results show that stanene/CrI$_3$ heterostructure has stronger interlayer vdW interaction than other vdW heterostructures, such as phosphorene/graphene [50], InSe/phosphorene [48], graphene/CrI$_3$ [40], and so on. Thus, there will be spin-polarized charges transfer between two layers, inducing spin-up electron and spin-down hole doping for CrI$_3$ layer and stanene layer, respectively.

Also, similar conclusions can be obtained from the perspective of the band alignment of heterostructure. The PBS show that the CrI$_3$ layer and stanene layer dominate the conduction band minimum (CBM) and the valence band maximum (VBM) in the spin-up channel, respectively. While for the spin-down channel, the CBM and VBM are both contributed by the stanene layer. These results indicate that the different spin states have different band alignments with type-II band alignment for the spin-up channel and type-I band alignment for the spin-down channel, which can lead to different transfer directions of electrons and holes at the interface in different spin states [51].

Since both the stanene and CrI$_3$ monolayer possess a strong SOC effect, we further calculate the band structure of stanene/CrI$_3$ FM vdWH considering the SOC effect, see Fig. 2(b). Interestingly, we find that the valley degeneracy of stanene at two inequivalent valleys ($K$ and $K'$ points in the first Brillouin zone) can be lifted. Namely, the valley polarization is produced in stanene by stacking on the FM monolayer CrI$_3$. For convenience, the degree of valley polarization can be marked as $\Delta E_{KK'} = |E_K - E_{K'}|$, which is the energy level difference between the $K$ and $K'$ points at the valence band edge. Here, the $\Delta E_{KK'}$ of stanene/CrI$_3$ FM vdWH is calculated as 39.6 meV, which is relatively large in the current known 2D valleytronics field. For example, the valley polarization of CrI$_3$/WSe$_2$ heterostructure is about $1 \sim 3$ meV in experiment and theory [27,52]. In addition, we also find that the bands of the stanene and CrI$_3$ have strong hybridization. The calculated results show that the CBM of stanene layer is composed of about 51% CrI$_3$ and 49% stanene, while the VBM is composed of about 23% CrI$_3$ and 77% stanene. Moreover, the spin-projection band structure of stanene/CrI$_3$ heterostructure along different spin components is displayed in Fig. S5 of the Supplemental Material [46]. The result shows that the spin polarized bands of stanene and CrI$_3$ not only have projections along the $z$ axis, but also have an in-plane component for the spin projections along the $x$ and $y$ axes. Based on the above results, the stanene/CrI$_3$ FM vdWH may be promising for the application of spintronic and valleytronic devices.

## C. Interlayer charge transfer in stanene/CrI$_3$ FM vdWH

In order to accurately confirm the interlayer charge transfer of stanene/CrI$_3$ FM vdWH, we further calculate the work functions, differential charge density, and perform the Bader charge analysis.

The work function is the difference between the vacuum level and the Fermi level. As shown in Figs. 3(a)–3(c), the
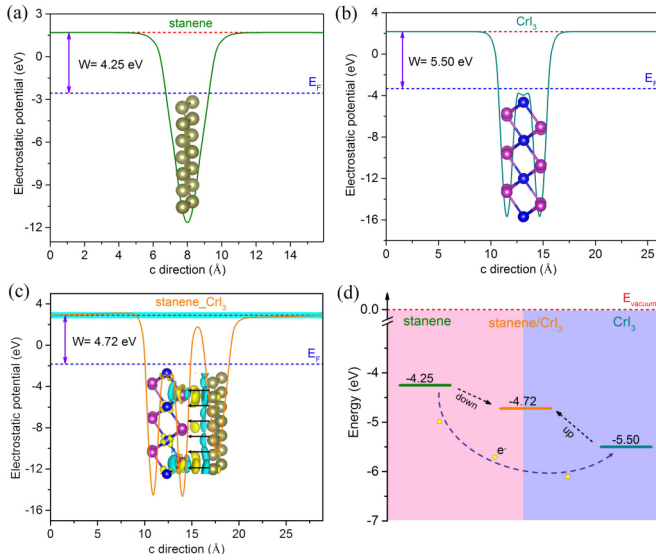
FIG. 3. The electrostatic potential of (a) stanene, (b) $CrI_3$ monolayer and (c) stanene/$CrI_3$ FM vdWH. (d) The transfer direction of electrons and the movement of the Fermi level in the process of forming heterostructure. The 3D surface of the charge density difference is also displayed in (c). The yellow and cyan areas represent electron accumulation and depletion, respectively, and the black arrows represent the direction of built-in electric field.

work functions of stanene, $CrI_3$ monolayer, and stanene/$CrI_3$ FM vdWH are 4.25, 5.50, and 4.72 eV, respectively. The smaller work function of stanene compared with $CrI_3$ indicates that the electrons can flow from stanene to $CrI_3$ when stanene comes into contact with $CrI_3$, see Fig. 3(d). As a result, the $CrI_3$ layer gathers negative charges, while the stanene layer accumulates positive charges, which is consistent with the above analysis about the hole doping in stanene and electron doping in $CrI_3$. Moreover, the work function of the stanene/$CrI_3$ FM vdWH is between that of stanene and $CrI_3$, which is due to the spontaneous charge transfer between two layers, lifting the Fermi levels of $CrI_3$ and stanene up and down, respectively, to achieve a balanced work function.

In Fig. 3(c), we also draw the 3D differential charge density of heterostructure in order to directly observe the charge transfer at the interface of heterostructure. The yellow and cyan areas represent electron accumulation and depletion, respectively, which can induce the built-in electric field at the interface, pointing from stanene layer to $CrI_3$ layer. The built-in electric field will hinder the spontaneous diffusion of electrons and holes induced by the work function difference, and resulting in a dynamic balance at the interface [53].

Also, the Bader charge analysis, a quantitative analysis, is performed in the stanene/$CrI_3$ FM vdWH, which shows that 0.706 electrons transfer from the stanene layer to the $CrI_3$ layer. Here, an average of 0.050 electrons are lost for per Sn atom, and 0.030 and 0.028 electrons are obtained for per Cr atom and I atom, respectively. This result is comparable to the theoretical results of other heterostructures, such as $FeI_2$/$In_2Se_3$ [54]. Recently, Zhou et al. have proved the interlayer charge transfer in $PtSe_2$/$MoSe_2$ heterostructure by the electrostatic force microscopy imaging in experiment [55]. We expect that the interlayer charge transfer in stanene/$CrI_3$
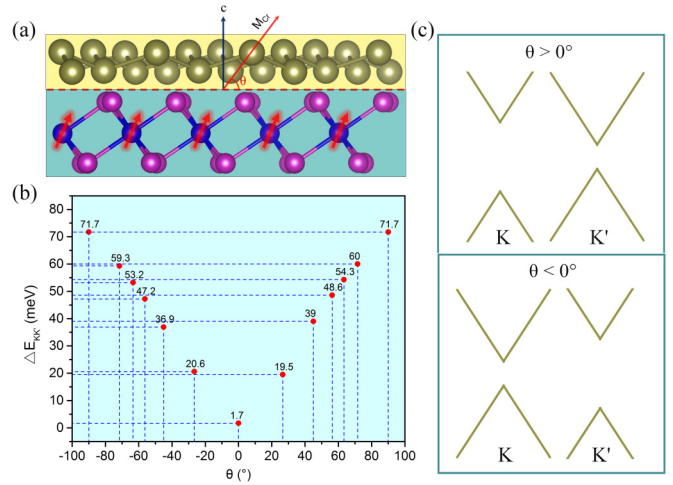


FIG. 4. (a) The side view of structure model of the stanene/$CrI_3$ FM vdWH. The right coordinate system represents the angle between the spin orientation of Cr atoms and the plane of heterostructure. (b) The values of valley polarization as a function of the angles ($\theta$) between the spin direction of Cr atoms and the plane of heterostructure. (c) A schematic diagram of the characteristics of valley polarization at $\theta > 0°$ and $\theta < 0°$.

can be confirmed through the above method. Thus, the interlayer charge transfer in stanene/$CrI_3$ FM vdWH is confirmed by different methods, suggesting the correctness of our results.

### D. Spin orientation controllable valley polarization in stanene/$CrI_3$ FM vdWH

For valley-polarized materials, how to well control the degree of valley polarization is very important for its practical application in valleytronic devices. It has been found that valley polarization can be regulated by external magnetic field in experiment, while the regulation scope of valley polarization is only 0.1–0.2 meV per Tesla by applying magnetic field [14,15]. Recently, monolayer $CrI_3$ has been found possesses a giant magneto band-structure effect, i.e. the spin orientation of Cr atoms can significantly modify the band structure of monolayer $CrI_3$ [56]. Based on this, we cannot help wondering whether the electronic structure of the stanene/$CrI_3$ FM vdWH can be affected by changing the spin orientation of Cr atoms.

Here, we define the angle between the spin direction of Cr atoms and the plane of heterostructure as $\theta$, see Fig. 4(a). The PBS of stanene in stanene/$CrI_3$ FM vdWH with the selected spin orientation are shown in Fig. 5. The calculation details for fixing the spin direction are provided in the Supplemental Material [46]. We also calculate the energy difference between different spin orientations, which shows that the total energy of the system is the lowest when the spin direction of Cr atom is parallel to the z axis (see Fig. S6 in the Supplemental Material [46]). In addition, the calculation results show that the magnetic moment of Cr atom changes from 3.369 $\mu_B$ to 3.488 $\mu_B$ when the stanene/$CrI_3$ heterostructure is formed. We also calculate the magnetic moment of Cr atom with different spin directions, showing that the magnetic moment
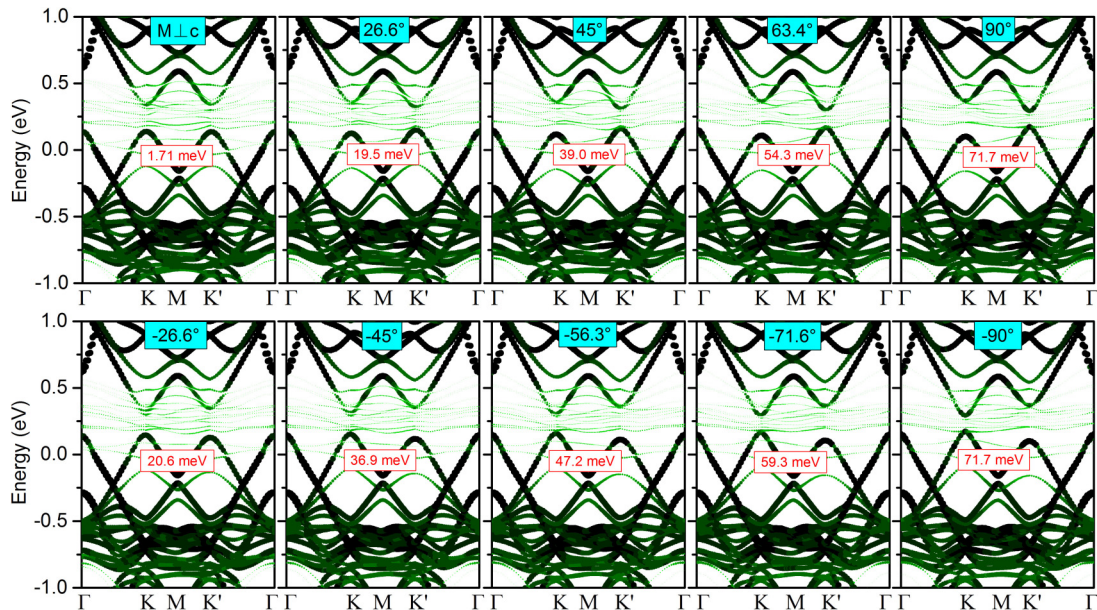
FIG. 5. The projected band structures of stanene with the effect of spin direction of the Cr atoms. The green and black colors denote the components of $CrI_3$ and stanene, respectively. The values in the blue boxes represent the angles between the spin direction of Cr atoms and the plane of heterostructure and the values in red boxes are the valley polarization values.

stays 3.488 $\mu_B$ when the spin orientation changes (see Fig. S7 in the Supplemental Material [46]).

Interestingly, we find that changing the spin orientation of Cr atoms can obviously affect the degree of valley polarization. The $\Delta E_{KK'}$ increases monotonously with increasing $\theta$, independent of the positive and negative direction of the $c$ axis, see Fig. 4(b). Moreover, the largest $\Delta E_{KK'}$ is reached with a value of 71.7 meV when the spin orientation of Cr atoms is parallel to the $c$ axis, while when the spin orientation of Cr atoms is perpendicular to the $c$ axis, the $\Delta E_{KK'}$ is decreased significantly, with the value only 1.7 meV. Also, it can be find that the spin orientation cannot only regulate the degree of valley polarization, but also modify the characteristics of valley polarization. As shown in Fig. 5, when $\theta > 0°$, the valence band level of $K'$ valley is higher than that of $K$ valley, while it is reversed when $\theta < 0°$. Figure 4(c) shows the relevant schematic diagram. Recently, Hong *et al.* have also found that the regulation of the valley-polarization characteristic can be achieved by applying external electric field [31]. However, regulating valley polarization by controlling the spin orientation is thought to be more essential for no external factors that may affect the performance of the material introduced in the system.

In experiments, the spin orientation of heavy metal elements with strong SOC effect can be regulated by applying in-plane current [57,58]. Moreover, the spin-orbit torque in stanene has been proved theoretically [59]. Thus, we can expect that the valley polarization of stanene/$CrI_3$ FM vdWH regulated by the spin orientation of Cr atoms can be realized in experiment.

## IV. CONCLUSION

In summary, through first-principles calculations, we theoretically realize obvious valley polarization ($\Delta E_{KK'} = 39.6$ meV) in stanene by stacking it on a 2D FM monolayer $CrI_3$ to form a heterostructure. We prove that the system is stable and owns the ferromagnetic ground state. Note that different stacking orders have little effect on its basic physical properties. When not considering the SOC effect, we find a spin-polarized Dirac electron behavior of stanene at the spin-down channel with an opened band gap (187.6 meV) and hole doping. More importantly, we find that the spin orientation of Cr atoms can significantly regulate the degree of valley polarization. When the spin orientation of Cr atoms is parallel to the $c$ axis, the $\Delta E_{KK'}$ can reach 71.7 meV, while the spin orientation is perpendicular to the $c$ axis, the $\Delta E_{KK'}$ is smallest with a value of 1.7 meV. These results indicate that stanene/$CrI_3$ FM vdWH is a promising candidate to design 2D high-performance spintronic and valleytronic devices.

[1] D. Xiao, W. Yao, and Q. Niu, Phys. Rev. Lett. **99**, 236809 (2007).

[2] D. Xiao, G.-B. Liu, W. Feng, X. Xu, and W. Yao, Phys. Rev. Lett. **108**, 196802 (2012).

[3] B. Zhu, H. Zeng, J. Dai, Z. Gong, and X. Cui, Proc. Natl. Acad. Sci. **111**, 11606 (2014).

[4] X.-P. Zhang, C. Huang, and M. A. Cazalilla, Phys. Rev. B **99**, 245106 (2019).

[5] Z. Wu, B. T. Zhou, X. Cai, P. Cheung, G.-B. Liu, M. Huang, J. Lin, T. Han, L. An, Y. Wang, S. Xu, G. Long, C. Cheng, K. T. Law, F. Zhang, and N. Wang, Nat. Commun. **10**, 611 (2019).

[6] E. Barré, J. A. C. Incorvia, S. H. Kim, C. J. McClellan, E. Pop, H.-S. P. Wong, and T. F. Heinz, Nano Lett. **19**, 770 (2019).

[7] T. Y. T. Hung, K. Y. Camsari, S. Zhang, P. Upadhyaya, and Z. Chen, Sci. Adv. **5**, eaau6478 (2019).

[8] Y. Wang, C. Cong, J. Shang, M. Eginligil, Y. Jin, G. Li, Y. Chen, N. Peimyoo, and T. Yu, Nanoscale Horiz. **4**, 396 (2019).

[9] A. Kareekunnan, M. Muruganathan, and H. Mizuta, Nanoscale **11**, 14707 (2019).

[10] X.-X. Zhang, Y. Lai, E. Dohner, S. Moon, T. Taniguchi, K. Watanabe, D. Smirnov, and T. F. Heinz, Phys. Rev. Lett. **122**, 127401 (2019).

[11] A. V. Kalameitsev, V. M. Kovalev, and I. G. Savenko, Phys. Rev. Lett. **122**, 256801 (2019).

[12] H. Zeng, J. Dai, W. Yao, D. Xiao, and X. Cui, Nat. Nanotechnol. **7**, 490 (2012).

[13] K. F. Mak, K. He, J. Shan, and T. F. Heinz, Nat. Nanotechnol. **7**, 494 (2012).

[14] G. Aivazian, Z. Gong, A. M. Jones, R.-L. Chu, J. Yan, D. G. Mandrus, C. Zhang, D. Cobden, W. Yao, and X. Xu, Nat. Phys. **11**, 148 (2015).

[15] D. MacNeill, C. Heikes, K. F. Mak, Z. Anderson, A. Kormányos, V. Zólyomi, J. Park, and D. C. Ralph, Phys. Rev. Lett. **114**, 037401 (2015).

[16] A. Arora, R. Schmidt, R. Schneider, M. R. Molas, I. Breslavetz, M. Potemski, and R. Bratschitsch, Nano Lett. **16**, 3624 (2016).

[17] R. Peng, Y. Ma, S. Zhang, B. Huang, and Y. Dai, J. Phys. Chem. Lett. **9**, 3612 (2018).

[18] J. Qi, X. Li, Q. Niu, and J. Feng, Phys. Rev. B **92**, 121403(R) (2015).

[19] X. Liang, L. Deng, F. Huang, T. Tang, C. Wang, Y. Zhu, J. Qin, Y. Zhang, B. Peng, and L. Bi, Nanoscale **9**, 9502 (2017).

[20] L. Xu, M. Yang, L. Shen, J. Zhou, T. Zhu, and Y. P. Feng, Phys. Rev. B **97**, 041405(R) (2018).

[21] N. Li, J. Zhang, Y. Xue, T. Zhou, and Z. Yang, Phys. Chem. Chem. Phys. **20**, 3805 (2018).

[22] G. Yang, J. Li, H. Ma, Y. Yang, C. Li, X. Mao, and F. Yin, Phys. Rev. B **98**, 235419 (2018).

[23] Q. Pei and W. Mi, Phys. Rev. Appl. **11**, 014011 (2019).

[24] B. Huang, G. Clark, E. Navarro-Moratalla, D. R. Klein, R. Cheng, K. L. Seyler, D. Zhong, E. Schmidgall, M. A. McGuire, D. H. Cobden, W. Yao, D. Xiao, P. Jarillo-Herrero, and X. Xu, Nature (London) **546**, 270 (2017).

[25] C. Gong, L. Li, Z. Li, H. Ji, A. Stern, Y. Xia, T. Cao, W. Bao, C. Wang, Y. Wang, Z. Q. Qiu, R. J. Cava, S. G. Louie, J. Xia, and X. Zhang, Nature (London) **546**, 265 (2017).

[26] Y. Deng, Y. Yu, Y. Song, J. Zhang, N. Z. Wang, Z. Sun, Y. Yi, Y. Z. Wu, S. Wu, J. Zhu, J. Wang, X. H. Chen, and Y. Zhang, Nature (London) **563**, 94 (2018).

[27] Z. Zhang, X. Ni, H. Huang, L. Hu, and F. Liu, Phys. Rev. B **99**, 115441 (2019).

[28] J. Xie, L. Jia, H. Shi, D. Yang, and M. Si, Jpn. J. Appl. Phys. **58**, 010906 (2019).

[29] K. L. Seyler, D. Zhong, B. Huang, X. Linpeng, N. P. Wilson, T. Taniguchi, K. Watanabe, W. Yao, D. Xiao, M. A. McGuire, K.-M. C. Fu, and X. Xu, Nano Lett. **18**, 3823 (2018).

[30] C. Lin, Y. Li, Q. Wei, Q. Shen, Y. Cheng, and W. Huang, ACS Appl. Mater. Interfaces **11**, 18858 (2019).

[31] M. U. Farooq and J. Hong, Npj 2D Mater. Appl. **3**, 3 (2019).

[32] Q. Pei, B. Zhou, W. Mi, and Y. Cheng, ACS Appl. Mater. Interfaces **11**, 12675 (2019).

[33] B. Zhou, Z. Li, J. Wang, X. Niu, and C. Luan, Nanoscale **11**, 13567 (2019).

[34] L. Matthes, O. Pulci, and F. Bechstedt, J. Phys. Condens. Matter **25**, 395305 (2013).

[35] S. Balendhran, S. Walia, H. Nili, S. Sriram, and M. Bhaskaran, Small **11**, 640 (2015).

[36] J. Qi, K. Hu, and X. Li, Phys. Rev. Appl. **10**, 034048 (2018).

[37] G. Kresse and J. Furthmüller, Comput. Mater. Sci. **6**, 15 (1996).

[38] J. P. Perdew, K. Burke, and M. Ernzerhof, Phys. Rev. Lett. **77**, 3865 (1996).

[39] A. I. Liechtenstein, V. I. Anisimov, and J. Zaanen, Phys. Rev. B **52**, R5467 (1995).

[40] J. Zhang, B. Zhao, T. Zhou, Y. Xue, C. Ma, and Z. Yang, Phys. Rev. B **97**, 085401 (2018).

[41] P. E. Blöchl, Phys. Rev. B **50**, 17953 (1994).

[42] H. J. Monkhorst and J. D. Pack, Phys. Rev. B **13**, 5188 (1976).

[43] D. Hobbs, G. Kresse, and J. Hafner, Phys. Rev. B **62**, 11556 (2000).

[44] S. Grimme, J. Comput. Chem. **27**, 1787 (2006).

[45] T. Kerber, M. Sierka, and J. Sauer, J. Comput. Chem. **29**, 2088 (2008).

[46] See Supplemental Material at http://link.aps.org/supplemental/10.1103/PhysRevB.100.195307 for the structural parameters, band structures of stanene and CrI$_3$ monolayer; the effect of lattice mismatch and stacking effect on band structure of stanene/CrI$_3$ heterostructure; the spin-projection band structure on stanene/CrI$_3$ heterostructure along the $x$, $y$, and $z$ axes, respectively; the effect of the spin orientation of Cr atom on the total energy of heterostructure and the magnetic moment of Cr atom; the method of fixing spin direction in Vienna Ab-initio simulation package.

[47] W.-B. Zhang, Q. Qu, P. Zhu, and C.-H. Lam, J. Mater. Chem. C **3**, 12457 (2015).

[48] J. E. Padilha, R. H. Miwa, A. J. R. da Silva, and A. Fazzio, Phys. Rev. B **95**, 195143 (2017).

[49] E. Voloshina and Y. Dedkov, J. Phys. Chem. Lett. **10**, 3212 (2019).

[50] J. E. Padilha, A. Fazzio, and A. J. R. da Silva, Phys. Rev. Lett. **114**, 066803 (2015).

[51] W. Xiong, C. Xia, J. Du, T. Wang, X. Zhao, Y. Peng, Z. Wei, and J. Li, Phys. Rev. B **95**, 245408 (2017).

[52] D. Zhong, K. L. Seyler, X. Linpeng, R. Cheng, N. Sivadas, B. Huang, E. Schmidgall, T. Taniguchi, K. Watanabe, M. A. McGuire, W. Yao, D. Xiao, K.-M. C. Fu, and X. Xu, Sci. Adv. **3**, e1603113 (2017).

[53] C.-X. Xia, J. Du, X.-W. Huang, W.-B. Xiao, W.-Q. Xiong, T.-X. Wang, Z.-M. Wei, Y. Jia, J.-J. Shi, and J.-B. Li, Phys. Rev. B **97**, 115416 (2018).

[54] W. Sun, W. Wang, D. Chen, Z. Cheng, and Y. Wang, Nanoscale **11**, 9931 (2019).

[55] J. Zhou, X. Kong, M. C. Sekhar, J. Lin, F. Le Goualher, R. Xu, X. Wang, Y. Chen, Y. Zhou, C. Zhu, W. Lu, F. Liu, B. Tang, Z.

Guo, C. Zhu, Z. Cheng, T. Yu, K. Suenaga, D. Sun, W. Ji, and Z. Liu, ACS Nano **13**, 10929 (2019).

[56] P. Jiang, L. Li, Z. Liao, Y. X. Zhao, and Z. Zhong, Nano Lett. **18**, 3844 (2018).

[57] Y. Fan, P. Upadhyaya, X. Kou, M. Lang, S. Takei, Z. Wang, J. Tang, L. He, L.-T. Chang, M. Montazeri, G. Yu, W. Jiang, T. Nie, R. N. Schwartz, Y. Tserkovnyak, and K. L. Wang, Nat. Mater. **13**, 699 (2014).

[58] L. Liu, O. J. Lee, T. J. Gudmundsen, D. C. Ralph, and R. A. Buhrman, Phys. Rev. Lett. **109**, 096602 (2012).

[59] H. Li, X. Wang, and A. Manchon, Phys. Rev. B **93**, 035417 (2016).